Understanding hysteresis in carbon dioxide sorption in porous metal-organic frameworks

DOI:
10.1021/acs.inorgchem.9b00016

Document Version
Accepted author manuscript

Published in:
Inorganic Chemistry

Understanding hysteresis in carbon dioxide sorption in porous metal-organic frameworks

Sergey A. Sapchenko,[*†,‡,§,#] *Marina O. Barsukova,*[†,‡,#] *Rodion V. Belosludov,*[⊥] *Konstantin A. Kovalenko,*[†,‡] *Denis G. Samsonenko,*[†,‡] *Artem S. Poryvaev,*[‡,¶] *Alena M. Sheveleva,*[‡,¶] *Matvey V. Fedin,*[‡,¶] *Artem S. Bogomyakov,*[‡,¶] *Danil N. Dybtsev,*[†,‡] *Martin Schröder,*[§] *and Vladimir P. Fedin*[†, ‡]

[†] Nikolaev Institute of Inorganic Chemistry, SB RAS, 630090, Novosibirsk, Russia

[‡] Novosibirsk State University, 630090, Novosibirsk, Russia

[§] School of Chemistry, University of Manchester, Oxford Road, M13 9PL, Manchester, UK

[⊥] Institute for Materials Research, Tohoku University, 980-8577, Sendai, Japan

[¶] International Tomography Center SB RAS, 630090, Novosibirsk, Russia

ABSTRACT

Two new isostructural microporous coordination frameworks $[Mn_3(Hpdc)_2(pdc)_2]$ (**1**) and $[Mg_3(Hpdc)_2(pdc)_2]$ (**2**) (pdc^{2-} = pyridine-2,4-dicarboxylate) showing primitive cubic (**pcu**) topology have been prepared and characterized. The pore aperture of the channels is too narrow for the efficient adsorption of N_2, however, both compounds demonstrate substantially higher

uptake of CO_2 (119.9 $ml \cdot g^{-1}$ for **1** and 102.5 $ml \cdot g^{-1}$ for **2** at 195 K, 1 bar). Despite of their structural similarities, **2** shows typical reversible type I isotherm for adsorption/desorption of CO_2, while **1** features a two-step adsorption process with a very broad hysteresis between the adsorption and desorption curves. This behavior can be explained by a combination of DFT calculations, sorption and XRD analysis and gives insights to the further development of new sorbents showing adsorption/desorption hysteresis.

INTRODUCTION

Carbon dioxide (CO_2) is a major anthropogenic contributor to the greenhouse effect. According to data from the World Meteorological Organization, the quantity of CO_2 in the atmosphere has grown at a record speed in 2016 to the highest level in 800 000 years, taking CO_2 in the atmosphere to 145% of pre-industrial levels.[1] To limit global warming to within 2°C greenhouse emissions need to be reduced by 40%–70% by 2050 and eliminated completely by 2100.[2] This will be especially difficult to achieve due to continued reliance upon fossil fuels, and thus the removal of CO_2 from the exhaust gas produced by power plants is a methodology to limit the growth of emissions. A typical flue gas contains up to 20 vol. % of carbon dioxide and various chemisorbents and physisorbents for its separation and storage are proposed up to date. Chemisorption based on trapping CO_2 with alkali and alkaline earth metal oxides (Na_2O, CaO, MgO),[3] composites based on aluminum oxide/oxohydroxide,[4,5] and tantalum oxide[6] or lithium silicates[7] have been reported. The use of organic bases such as monoethanolamine (MEA), diethanolamine (DEA) and methyldiethanolamine (MDEA) in aqueous solution is another effective method for chemical capture of CO_2.[8]

Capture and separation of CO_2 by physisorption involves weaker bonding energetics and can thus be applied to cyclic adsorption/desorption processes, with desorption induced by changes in pressure or by heating. Zeolites,[9–11] activated carbon,[12,13] metal-organic frameworks (MOFs),[14–18] zeolitic imidazolate frameworks (ZIFs)[19] and covalent-organic frameworks materials (COFs)[20–22] are the most prominent solid adsorbents considered for CO_2 capture by physisorption. Many of these materials demonstrate one-step type I sorption isotherms with CO_2 indicating a typical Langmuir sorption mechanism. Recently, McDonald *et al*. demonstrated the advantages of sorbent exhibiting stepped isotherms, with S-shaped hysteresis for CO_2 uptake and release.[23] In contrast to classical solid sorbents and reference amine systems, materials showing significant hysteresis can be regenerated with lower energy penalties and have greater working capacities. Thus, the development of solid-state materials showing hysteresis is highly desirable for efficient CO_2 uptake and capture; however, the systematic design of such systems is restrained by lack of understanding of the mechanisms leading to the high hysteresis in CO_2 sorption.

We report the synthesis and characterization of two multifunctional porous MOF complexes, $[Mn_3(Hpdc)_2(pdc)_2]$ (**1**) and its isostructural analogue $[Mg_3(Hpdc)_2(pdc)_2]$ (**2**) (pdc^{2-} is pyridine-2,4-dicarboxylate). In spite of their close structural similarities, **2** shows rather typical reversible CO_2 adsorption isotherm while **1** features extremely high adsorption/desorption hysteresis and high selectivity to CO_2 over N_2 and CH_4. A detailed investigation of their gas sorption, magnetic and luminescent properties allowed us to determine the fundamental mechanism of the surprisingly high CO_2 hysteresis in **1** by a combination of experimental and theoretical methods.

EXPERIMENTAL SECTION

Materials and Measurements. All reagents and solvents were commercially available and used as supplied without further purification. The FTIR spectra were recorded from KBr pellets in the range 4000–400 cm^{-1} on Scimitar FTS 2000 Fourier-transform infrared spectrometer. Thermogravimetric analysis (TGA) was performed using TG 209 F1 Iris Thermo Microbalance (NETZSCH) instrument at temperatures between 25 and 600°C under He atmosphere at a heating rate of 10°C/min. Powder X-ray diffraction (PXRD) patterns were measured with Cu-Kα radiation on a Shimadzu XRD 7000S powder X-ray diffractometer. Elemental analyses (C, H, N) were performed on the Euro EA 3000 CHN Elemental Analyzer.

$[Mn_3(Hpdc)_2(pdc)_2]\cdot 4.8DMF\cdot H_2O$ (1). Pyridine-2,4-dicarboxylic acid monohydrate (H_2pdc) (185 mg, 1 mmol), $MnCl_2\cdot 4H_2O$ (148 mg, 0.75 mmol) and triethylamine (2 mmol, 280 µl) were dissolved in N,N-dimethylformamide (DMF) (20 mL) containing concentrated HCl (15 drops) in a 25 mL screwed-cap glass vial. The reaction was heated at 100 °C for 3 days and the mixture cooled to room temperature. The yellow crystals were filtered and washed with DMF (1 ml) three times. Yield: 47% (based on Mn). Elemental analysis. Calcd (%) for $C_{42.4}H_{49.6}Mn_3N_{8.8}O_{21.8}$: C 42.8, H 4.2, N 10.3; found (%): C 43.5, H 4.6, N 9.9. IR spectra see Figure S1. Phase purity of the crystals was confirmed by powder X-ray diffraction (PXRD) (Figure S1).

$[Mg_3(Hpdc)_2(pdc)_2]\cdot 4DMF\cdot H_2O$ (2). 2 was obtained according to the procedure used for compound **1**. Pyridine-2,4-dicarboxylic acid monohydrate (H_2pdc) (185 mg, 1 mmol), $Mg(NO_3)_2\cdot 6H_2O$ (128 mg, 0.5 mmol) and triethylamine (2 mmol, 280 µl) were dissolved in N,N-dimethylformamide (DMF) (20 mL) containing concentrated HCl (15 drops) in a 25 mL screwed-cap glass vial. The reaction was heated at 100 °C for 3 days and the mixture cooled to

room temperature. The colorless crystals were filtered and washed with DMF (1 ml) three times. Yield: 45% (based on Mg). Elemental analysis. Calcd (%) for $C_{40}H_{46}Mg_3N_8O_{22}$: C 45.2, H 4.4, N 10.5; found (%): C 46.0, H 5.0, N 10.2. IR spectra see Figure S1. Phase purity of the crystals was confirmed by powder X-ray diffraction (PXRD) (Figure S1).

Crystallographic studies. Single crystal X-ray diffraction data of **1** were collected at 150 K on a Bruker Apex Duo automatic four-circle diffractometer equipped with an area detector (Cu-Kα, λ = 1.54178 Å, graphite monochromator, φ and ω scans). Data collection, frame integration, and data processing were performed with the use of the APEX2 and SAINT program packages.[24] The absorption correction was applied based on the intensities of equivalent reflections with the use of the SADABS program.[24] The structure was solved by direct method and refined on F^2 by full-matrix least-squares method in the anisotropic approximation (for non-hydrogen atoms) using SHELX-2014 program package.[25] The positions of hydrogen atoms of organic ligands were calculated geometrically and refined by a riding model. Guest DMF and water molecules in the structure **1** are highly disordered and were not refined as a set of discrete atoms. The PLATON/SQUEEZE[26] procedure was applied to calculate the contribution to the diffraction from the solvent region and thereby produced a set of solvent-free diffraction intensities. The final composition of the compound was calculated taking into account the SQUEEZE results (333 e^- in 1235.3 Å^3). Residual electron density (3.19 e/Å^3) in the structure of **1** is situated close to Mn(2) and O(21) atoms (1.65–1.18 Å). A summary of the crystallographic data and structural determination for **1** is provided in Table S1, and selected bond length and angles are listed in Table S2. The unit cell parameters calculated from PXRD data are given in Table S3.

CCDC 1853065 contains the supplementary crystallographic data for this paper. These data can be obtained free of charge from The Cambridge Crystallographic Data Center at http://www.ccdc.cam.ac.uk/data_request/cif.

DFT calculations: First-principles calculations were performed within the framework of density functional theory (DFT) as implemented in the Vienna Ab initio Simulation Package (VASP).[27,28] The Perdew, Burke, and Ernzerhof (PBE) parameterization of generalized gradient approximation (GGA) and the all-electron projector augmented wave (PAW) method to model the interactions between the ion cores were used.[29,30] The plain-wave cutoff energy was 400 eV and convergence in energy (10^{-4} eV) and force (3×10^{-3} eV/Å) were used during the optimization procedure. Monkhorst-Pack *k*-point mesh of 3 × 3 × 3, was used for Brillouin zone integration,[31] and the semiempirical dispersive van der Waals (vdW) interaction was taken into account using the Grimme parametrization.[32] The difference between the energy of adsorbed system $(E_{host+guest})$ and the sum of the energies of the empty metal-organic framework (E_{host}) and the number of non-coordinated guest molecules $(n*E_{guest})$, with *n* equal to the number of adsorbed molecules was used in order to estimate the adsorption energies (E_{ads}) using the following expression

$$E_{ads} = E_{host+guest} - (E_{host} + n*E_{guest}). \quad (\mathbf{1})$$

A negative value of E_{ads} indicates that the adsorption state is thermodynamically favourable. The host–guest interaction has been demonstrated by the difference in charge density (excess and depletion electrons) given by

$$\Delta\rho = \rho(\text{host+guest}) - \rho(\text{host}) - \sum_{k=1}^{n} \rho_k(\text{guest}). \quad (\mathbf{2})$$

All structures of the MOF with adsorbed guest molecules as well as the obtained charge density isosurfaces for the guest-host interactions were visualized by using VESTA code.[33] The methods and theoretical analysis described have been verified in our previous studies of gas sorption into MOF structures.[34,35] The effective charge of atoms was evaluated by using the Bader analysis algorithm.[36-39]

Luminescence studies. The excitation and emission spectra of the solid samples were recorded on a Cary Eclipse (Varian) fluorescence spectrophotometer. The emission spectra of the complexes were recorded at room temperature under the following experimental conditions: V = 500 V, spectral slit width = 5 nm. The Xenon flash lamp was used as a light source to excite the steady-state PL spectra.

Activation procedure. Crystals of **1** and **2** were soaked in acetone for 3 days, dried and placed under vacuum at room temperature for 12 h in a Quantachrome Autosorb iQ volumetric instrument. The activated compounds retain their crystallinity after sorption experiments, according to PXRD (Figure S2).

Gas adsorption studies. Gas isotherms were measured on a Quantachrome Autosorb iQ volumetric instrument using a cryocooler. N_2 at 77 K and CO_2 at 195 K sorption–desorption isotherms were measured in the range 10^{-4} to 1 bar.

In situ **Synchrotron Powder X-ray Diffraction (PXRD).** *In situ* PXRD experiments were carried out at Beamline I11 Diamond Light Source (Oxford, UK) as a function of CO_2 loading using high-resolution synchrotron diffraction (λ = 0.825774 Å). The sample was loaded into capillary gas cell, and the temperature controlled by an Oxford open-flow Cryosystems. Activated **1** was generated by heating the sample *in situ* under vacuum overnight. The resultant PXRD was measured at 0, 0.25, 0.5 and 1 bar of CO_2 pressure at 195 K.

Magnetic measurements. The magnetic susceptibility of the polycrystalline samples was measured on a Quantum Design MPMS*XL* SQUID magnetometer over the temperature range 2–300 K with magnetic field of up to 5 kOe. Diamagnetic corrections were made using the Pascal constants. The effective magnetic moment was calculated as

$$\mu_{eff}(T) = [(3k/N_A\mu_B^2)\chi T]^{1/2} \approx (8\chi T)^{1/2} \quad (3)$$

EPR measurements. Polycrystalline powder (5 mg) of activated compound was placed in the an EPR sample tube (OD 2.8 mm ID 1.8 mm) and evacuated at room temperature and low pressure (10^{-5} torr) over 24 h. The desired amount of gas was introduced and the sample cooled with liquid N_2 and the sample was sealed. All data were obtained using Bruker ELEXYS E580 spectrometer at Q-band (≈34 GHz) equipped with temperature control system. The best trade-off between sensitivity, resolution and avoiding saturation was found by measuring FID-detected EPR spectra at 20 K, and then applying pseudomodulation of 0.1 mT. Figure S9 shows qualitative simulation of the FID-detected EPR spectra of samples **1** and **3**. In both cases, in agreement with structural data, model assumes superposition of two centers: MnO_6 with only ^{55}Mn hyperfine interaction (HFI) constant, and MnO_4N_2 with ^{55}Mn HFI and two ^{14}N HFIs. The calculated spectra were obtained using the following parameters:

MnO_6 unit: A(^{55}Mn) = 9.0 mT, g = 2.002.

MnO_4N_2 unit: A(^{55}Mn) = [9.0 9.0 8.8] mT, g = [2.002 2.002 1.998], A(^{14}N)=[0.5 1.5 2.0] mT.

To simulate broadening of the spectrum of samples 3 vs. 1, we imposed additional line broadening in 3 equivalent of the linewidth of 0.5 mT.

RESULTS AND DISCUSSION

Yellow prismatic crystals of $[Mn_3(Hpdc)_2(pdc)_2]\cdot 4.8DMF\cdot H_2O$ (**1**·4.8DMF·H_2O) were obtained by heating $MnCl_2\cdot 4H_2O$ and 2,4-pyridinedicarboxylic acid in the presence of small amounts of triethylamine in a slightly acidified N,N-dimethylformamide. **1**·4.8DMF·H_2O crystallizes in the orthorhombic space group *Pba*2 (Table S1), and comprises two crystallographically independent Mn(II) ions and two pyridinedicarboxylate ligands (Figure 1).

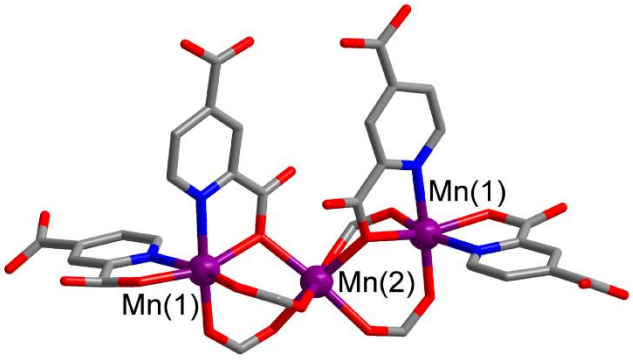

Figure 1. Structure of secondary building unit in $[Mn_3(Hpdc)_2(pdc)_2]$ (**1**).

The Mn(II) centers show distorted octahedral coordination with Mn(1) bound to four O and two N centres, and Mn(2) bound to six O atoms from six pyridinedicarboxylate ligands. All the Mn–N and Mn–O bond lengths fall within the range for other octahedral complexes of Mn(II) (Table S2). Each Mn(2) center connects to two Mn(1) atoms via μ-carboxylate groups to form a trinuclear $\{Mn_3(OOC)_6N_6\}$ unit, which can be regarded as 6-connected node bound to $Hpdc^-$ /pdc^{2-} linkers into layers in the *ab* plane. Another pdc^{2-} ligand connects these layers in three dimensions to give a framework of **pcu** topology, which comprises a system of intersected channels with an aperture of 3×6 Å (Figure 2).

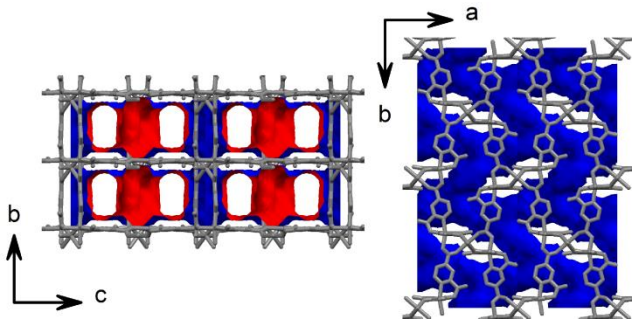

Figure 2. View of the pore in $[Mn_3(Hpdc)_2(pdc)_2]$ (**1)** along the *a* and *c* axes.

The free accessible volume estimated by PLATON[26] is 49%. In the as-synthesized material the pores are filled with disordered solvent molecules of DMF and H_2O. According to the TGA and elemental analytical data and the results of the SQUEEZE procedure[26] the chemical composition of the as-synthesized form is $[Mn_3(Hpdc)_2(pdc)_2]\cdot 4.8DMF\cdot H_2O$. The phase purity of the bulk sample of compound **1**$\cdot 4.8DMF\cdot H_2O$ was confirmed by PXRD (Figure S1). It is important to note that the charge balance of **1** was unambiguously assigned to a combination of pdc^{2-} and $Hpdc^-$ ligands rather than to higher oxidation Mn(III) or Mn(IV) states by magnetic measurements (*vide infra*) and by bond valence sum analysis.[40]

The colorless microcrystalline $[Mg_3(Hpdc)_2(pdc)_2]\cdot 4DMF\cdot 2H2O$ (**2**$\cdot 4DMF\cdot 2H_2O$) was obtained under analogous reaction conditions to **1** using $Mg(NO_3)_2$ as a metal source. The PXRD patterns for **2** and **1** coincide, confirming the isostructural nature of both compounds (Figure S1). The indexing of the peaks gave very similar unit cell parameters (Table S3).

1 and **2** show similar thermal behavior (Figure S4) under He with weight loss occurring in up to 320 and 300°C, respectively, assigned to the loss of guest water and DMF molecules. Both compounds demonstrate the same weight loss of 31% consistent with their formulation. This first

weight loss is followed by a plateau region ranging up to 400 and 460°C for **1** and **2**, respectively, confirming their chemical with further heating leading to decomposition of the frameworks.

As might be expected for materials containing different metal cations, **1** and **2** show different luminescent properties. The excitation and emission spectra are displayed on Figure 3. For as-synthesized **1**, the emission spectrum displays a greenish-yellow color with a broad band centered at 580 nm assigned to a ligand-to-metal electronic transition. The emission spectra of as-synthesized **2** shows band at 420 nm, assigned to intra-ligand pyridinedicarboxylate-centered electronic transition. Thus, the electron ligand-to-metal charge transfer was observed only in the case of compound **1**, since *d*-orbitals of Mn centers can participate in the charge transfer,[41,42] while charge-transfer emission is not characteristic for the compounds of *s*-elements such as Mg.

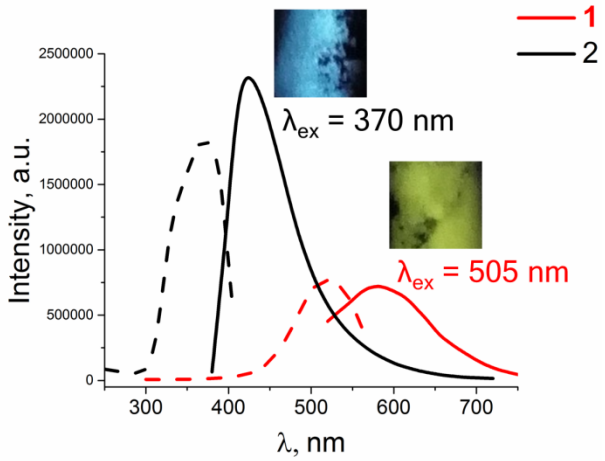

Figure 3. Solid-state luminescence spectra of $[Mn_3(Hpdc)_2(pdc)_2]$ **1** (λ_{ex}=505 nm) and $[Mg_3(Hpdc)_2(pdc)_2]$ **2** (λ_{ex}=370 nm). Excitation spectra are shown with dashed lines; emission spectra are shown with solid lines.

Removal of guest water and DMF molecules was achieved by soaking **1** and **2** in acetone for several days and then placed under vacuum at ambient conditions. The PXRD pattern (Figure

S2) and elemental analytical data confirm removal of guest molecules and retention of the framework structure after sorption. However, N_2 sorption experiments at 77 K (Figure S5) show very low adsorption even at 1 bar, with uptakes of 36.4 mL/g for **1** and 32.5 mL/g for **2**. CO_2 has a smaller kinetic diameter than N_2, and CO_2 uptake was found to be 119.9 mL/g for **1** and 102.5 mL/g for **2** at 195 K and 1 bar (Figure 4).

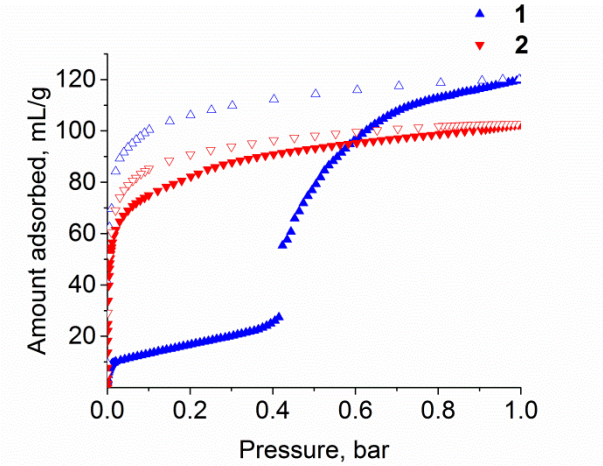

Figure 4. View of the adsorption (filled symbols) and desorption (open symbols) isotherms at 195 K for CO_2 in $[Mn_3(Hpdc)_2(pdc)_2]$ **1** (blue triangles) and $[Mg_3(Hpdc)_2(pdc)_2]$ **2** (red triangles).

For **2** the CO_2 sorption isotherm at 195 K has a typical type I shape with a small degree of sorption/desorption hysteresis. The BET surface area for **2** was measured as 383 $m^2 \cdot g^{-1}$ (Table 1). The general shape of the isotherm does not change with increasing temperature and only leads to the expectedly lower CO_2 uptake (Figure 5). Overall, **2** demonstrates the classical behavior of a microporous solid. However, the sorption isotherm for CO_2 in **1** collected at various temperatures has a stepwise S-shaped form with a very large hysteresis loop, which is less common for microporous materials (Figure 5).

Table 1. Parameters for the porous structures **1** and **2**.

Compound	Specific surface area / $m^2 \cdot g^{-1}$			V_{pore} / $cm^3 \cdot g^{-1}$		$V_{ads}(N_2)^a$/ $cm^3(STP) \cdot g^{-1}$
	Langmuir	BET	DFT	Gourvich	DFT	
1	594[b]	520[b]	107	0.251	0.023	120
2	476[b]	383[b]	660	0.215	0.149	102

[a] measured or calculated at P = 1 bar

[b] calculated from desorption curve for CO_2.

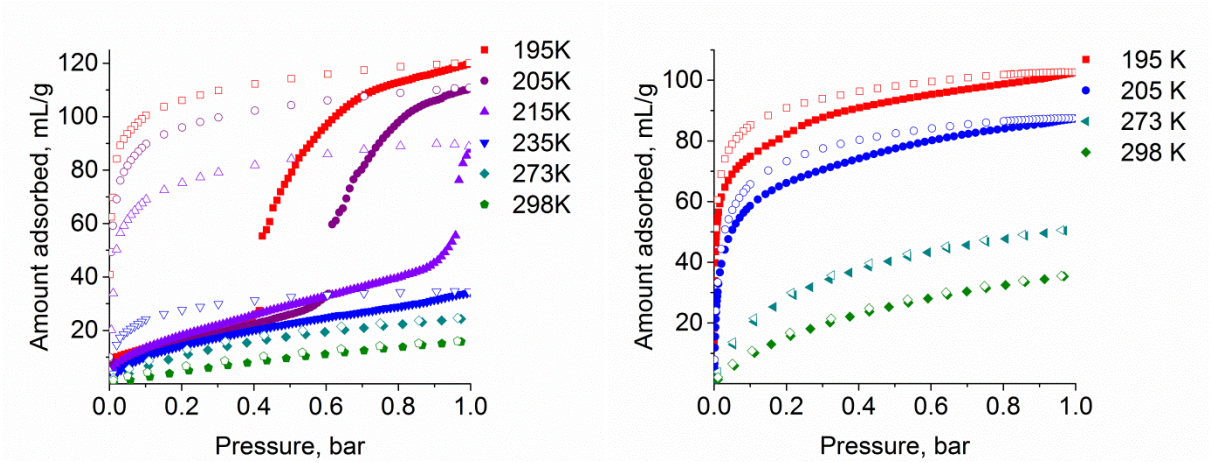

Figure 5. View of the adsorption (filled symbols) and desorption (open symbols) isotherms at different temperatures for CO_2 in $[Mn_3(Hpdc)_2(pdc)_2]$ **(1)** (left) and $[Mg_3(Hpdc)_2(pdc)_2]$ **(2)** (right).

The CO_2 sorption isotherm at 195 K has two steps. The first step lies in the low-pressure region and is characterized by low gas uptake (26.0 mL/g of CO_2 at 0.4 bar). With increasing pressure there is a dramatic growth of the CO_2 uptake reaching 119.9 mL/g at 195 K and 1 bar. At the same time the gas-saturated sample of **1** demonstrates practically no desorption until the pressure drops to 0.1 bar, when an abrupt release of a large amount of CO_2 takes place, resulting

in a very high sorption/desorption hysteresis. The absorbed CO_2 cannot be completely released even at low pressures, indicating a strong interaction between CO_2 and the framework **1** at 195 K which could be described in terms of quadrupole interactions between guest molecules and the framework.[43] Approximation of the desorption isotherm with a virial equation gives a surface area of 520 $m^2 \cdot g^{-1}$ for **1** (Table 1). It is important to note all isotherms are fully reversible and reproducible for different batches of samples **1** and **2**.

To quantitatively characterize the sorption hysteresis in **1** the hysteresis extent (*HE*) was calculated as following:

$$HE = \frac{S_{des} - S_{ads}}{S_{ads}} \cdot 100\% = \frac{\int_p m_{des}(p)dp - \int_p m_{ads}(p)dp}{\int_p m_{ads}(p)dp} \cdot 100\%$$

where $m_{des}(p)$, $m_{ads}(p)$ are the uptake functions of pressure for desorption and adsorption respectively and S_{des}, S_{ads} are the areas under desorption and sorption corves in *m-p* coordinates. The obtained values of HE are very high and are among the highest values obtained for the materials with huge hysteresis loops (Table 2).

Table 2. Hysteresis Extent in the sorption isotherms of CO_2 in **1** and other MOFs at different temperatures.

Compound Name/Formula	Temperature, K	*HE*, %	ref.
1	195	68	This article
	205	110	
	215	165	
	235	41	

$[Cu_2(glu)_2(bpy)]$	298	13	44
$[Cu_2(glu)_2(bpe)]$	298	21	
$[Cu_2(glu)_2(bpymh)]$	298	3	
$[Zn_2(DB\text{-}bdc)_2(dabco)]$	195	173	45
$[Zn_2(BPy\text{-}bdc)_2(dabco)]$	195	70	
BMOF-1-dcppy	196	94	46
[Zn(glu)(μ-bpe)]	196	15	47
NOTT-202a	195	39	48
	221	0	
JLU-Liu4	195	41	49
$\{[Co_2(ndc)_2(bpee)_2](bpee)\}$	195	7	50
ITF-1	273	42	51
YO-MOF	273	61	52
$[La(btb)(H_2O)]$	278	37	53

Notably, the second adsorption step is consistently observed when the CO_2 adsorption reaches *ca*. 25 mL/g corresponding to 1 molecule of CO_2 per formula unit of **1**. The position of the hysteresis loop in the adsorption isotherm moves to higher pressure with increasing temperature, and results in a non-linear dependency of *HE* with temperature (Table 2). *HE* grows with temperature to reach a maximum of 165% at 215 K. It then decreases to 41% at 235 K with no hysteresis observed at 298 K. Generally the value of HE decreases linearly with pressure, with the position of the S-step shifting to the higher pressure region as in the case of NOTT-202a.[44] The shift of the hysteresis loop also affects the sorption capacity of the material at 1 bar. Indeed, at 273 K and 235 K **1** adsorbs 25.3 mL/g and 34.3 mL/g of CO_2 respectively. Moreover, the hysteresis extent in **1** is comparable to $[Zn_2(DB\text{-}bdc)_2(dabco)]$, which has the highest reported

HE.[41] The hysteretic sorption/desorption in the latter originates from a phase transition upon the introduction of CO_2.

To investigate these possible structural rearrangements we performed *in situ* PXRD studies of activated **1** at 195 K (Figure S6) at 0, 0.25, 0.5 and 1 bar and then back to 0.5 bar and 0. The PXRD analysis of **1** with CO_2 revealed no phase transition. Thus, the value of *HE* for **1** with CO_2 is the highest for a material that does not undergo any phase-transformation during the adsorption/desorption cycle, and suggests the formation of stronger bonding to adsorbed CO_2 molecules within the pore.

The previously reported microporous materials $[Mn(HCOO)_2]$[54] and $[Mg(HCOO)_2]$[55] have identical structures and demonstrate the same sorption behavior unlike compounds **1** and **2**. The classical model of host-guest electrostatic interactions between CO_2 and the framework cannot explain the origin of the high hysteresis in **1** and its absence in case of compound **2** as well. In order to explain the different gas sorption behavior in **1** and **2**, we have performed the extensive DFT simulations of their CO_2 adsorption. For both compounds, we tracked the energetics and the location of the adsorbed CO_2 molecules by gradual molecule-by-molecule interaction with the framework to reveal the sorption pathway.

To begin with the most stable position for a single CO_2 was determined among the various guest positions inside the MOF channel for **1** and **2** as shown on Figure S7. The results indicate that the CO_2 molecule interacts differently in **1** and **2** at the initial stage of the sorption process. In the case of **1**, the guest molecule is located parallel to the pyridine ring along the *b* axis and lies perpendicular to *c* axis as shown on Figure 6a. The charge density isosurface shows charge redistribution in the adsorbed CO_2 molecule (Figure 6c) as well as significant charge redistribution in the host framework indicating a strong guest-host interaction with

$[Mn_3(Hpdc)_2(pdc)_2]$. In the case of compound **2**, the guest molecule is located perpendicular to the pyridine ring lying in the *ac* plane at a slight inclination due to a localized interaction between the carbon atom of CO_2 and oxygen atom of the carboxyl group of nearest pyridinedicarboxylate ligand (Figure 6b). The excess charge is localized on both O-atoms of adsorbed CO_2 and the carboxyl group of nearest pyridinedicarboxylic ligand; electron depletion occurs on the lower pyridinedicarboxylic ligand and on the C-atom of CO_2 (Figure 6d). This results in a higher value for the energy of adsorption of CO_2 in **2** at an uptake of 1 molecule per formula unit (see Table 3).

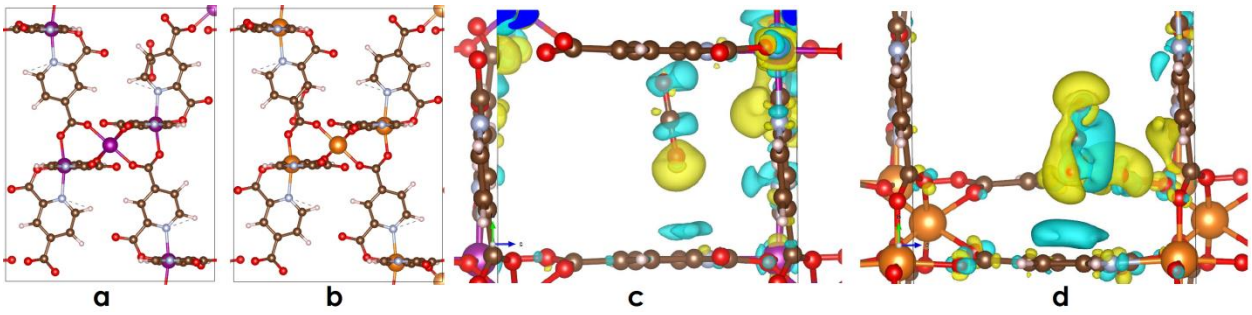

Figure 6. View of the most favorable intermolecular interactions and guest position of CO_2 in (a) $[Mn_3(Hpdc)_2(pdc)_2]$ **1** and (b) $[Mg_3(Hpdc)_2(pdc)_2]$ **2**. Charge density isosurfaces for the interactions of CO_2 with (c) $[Mn_3(Hpdc)_2(pdc)_2]$ **1** and (d) $[Mg_3(Hpdc)_2(pdc)_2]$ **2**. Yellow represents the accumulation of electron density and green the depletion of electron density. The DFT results are visualized using the VESTA code.

Table 3. The adsorption energy (E_{ads}) of CO_2 into $[Mn_3(Hpdc)_2(pdc)_2]$ (**1**) and $[Mg_3(Hpdc)_2(pdc)_2]$ (**2**) as calculated by DFT calculations. Values per single molecule are in parentheses.

Entry of n × Guest	**1**	**2**
	E_{ads} / kcal/mol	
1×CO_2	–6.370 (–6.370)	–7.160 (–7.160)
2×CO_2	–12.72 (–6.360)	–12.36 (–6.180)
3×CO_2	–20.86 (–6.953)	–17.76 (–5.920)
4×CO_2	–25.90 (–6.475)	–23.46 (–5.865)

We then studied the gradual molecule-by-molecule interaction of the framework with guest CO_2 molecules and the most stable configurations. The calculations revealed the presence of several CO_2 adsorption sites I – IV (Figure 7) in the low pressures region. Sites I-IV are common for the both frameworks, however the order in which these sites are filled by CO_2 molecules is different. In **2** the first 4 CO_2 molecules (per formula unit) form a chain-like. The chain-like CO_2 superstructure was also observed for **1**, yet the site III not I is the first that is occupied by guest CO_2 molecule. The introduction of the next CO_2 molecules into the framework results in rearrangement of the guest species with CO_2 occupying the sites I and II. Thereupon a very similar chain to the one observed in **2** is formed at higher CO_2 loadings. These interesting chain-like superstructures for CO_2 are stabilized through guest-exchange interactions shown in Figure 7.

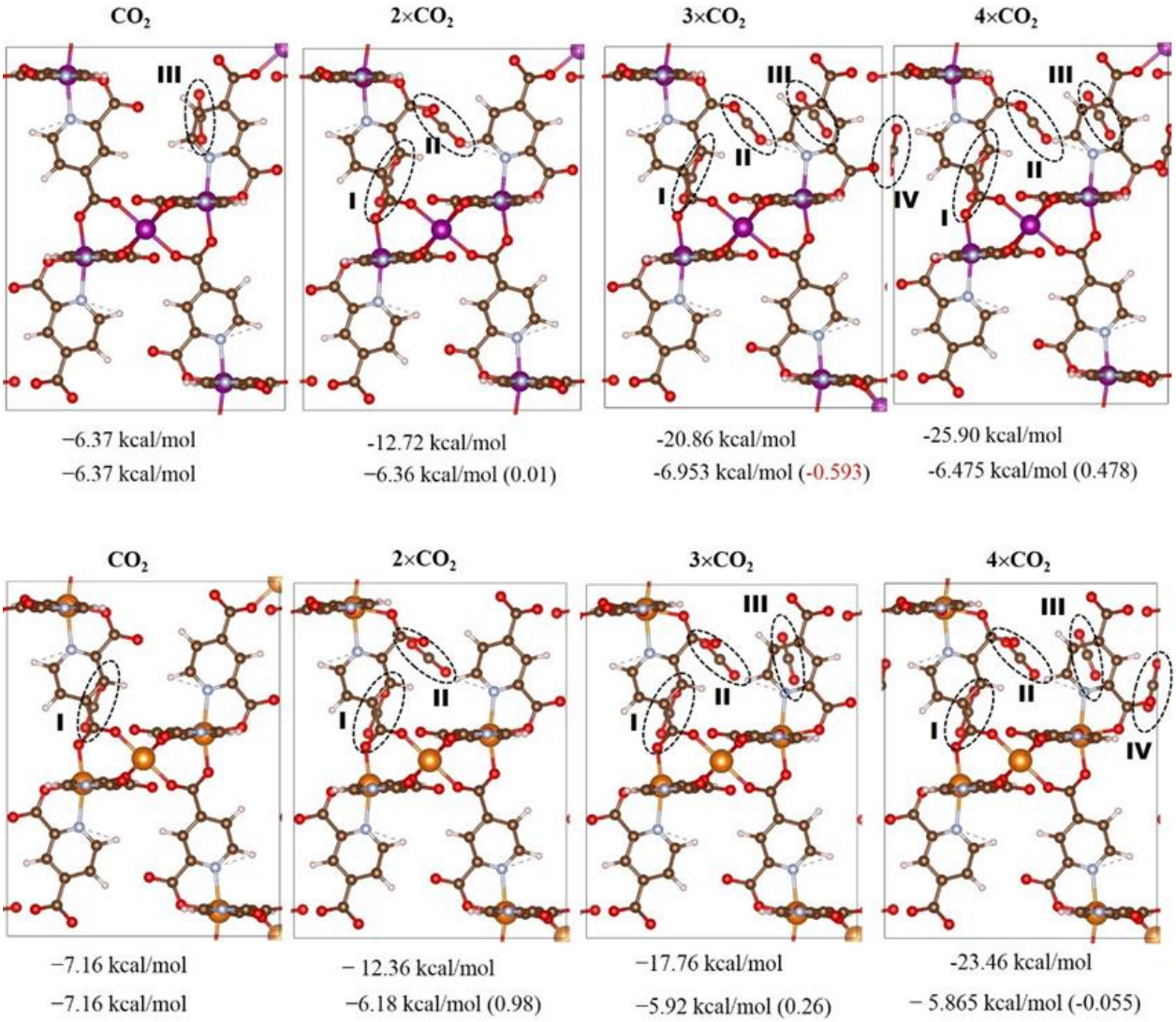

Figure 7. View of calculated adsorption sites in $[Mn_3(Hpdc)_2(pdc)_2]$ (**1**) (up) and $[Mg_3(Hpdc)_2(pdc)_2]$ (**2**) (bottom).

The charge density isosurface corresponds to the stable chain-like configuration achieved by electrostatic interactions *via* the excess and depletion of electron density localized on the O- and C-atoms of CO_2, respectively. Indeed, the importance of electrostatic interaction between CO_2 proposed has been proposed previously,[56,57] but never visualized in the manner shown on Figure 8.

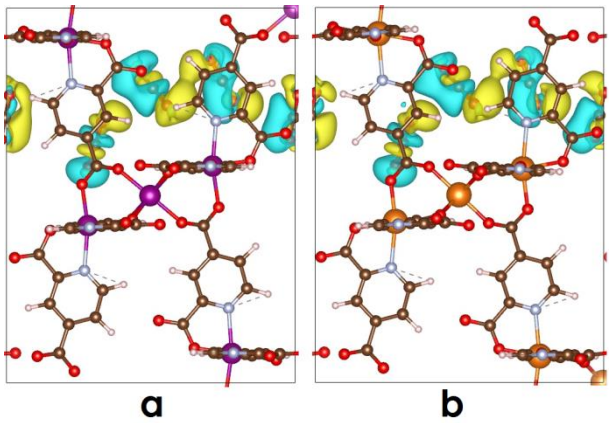

Figure 8. View of charge density isosurfaces for the guest-guest interactions of 4×CO_2 inside (a) [$Mn_3(Hpdc)_2(pdc)_2$] **1** and (b) [$Mg_3(Hpdc)_2(pdc)_2$] **2**. Yellow represents the accumulation of electron density and green the depletion of electron density.

Importantly, **1** and **2** show different thermodynamics of formation of the CO_2 chains. To understand this effect we plotted the energy difference of interaction between a single CO_2 molecule and the two frameworks, and examined different possible positions of the guest species (Figure 9). To explain the clear difference in position of the first occupied site, as well as in the energetics of single-molecule adsorption sites 2 and 9 we performed additional calculations of local geometry and electronic structure of CO_2. The data on partial density of states (PDOS) revealed compound **1** to demonstrate metallic features due to the presence of 3*d* electrons from manganese atoms near the Fermi level (Figure S8, *a*), while compound **2** was found to be a semiconductor due to the absence of *d*-electrons (Figure S8, *b*). Given this, one can expect the lesser impact of metallic centers in **2** on the overall process of the adsorption. Indeed, the introduction of the CO_2 molecules did not change significantly the electronic structure of the MOF complex (Figure S9), therefore we can assume pure electrostatic interaction between CO_2 molecules and the framework plays a decisive role here. The largest overlapping between the CO_2 molecular orbitals with the framework were found for the position 9 within the energy range

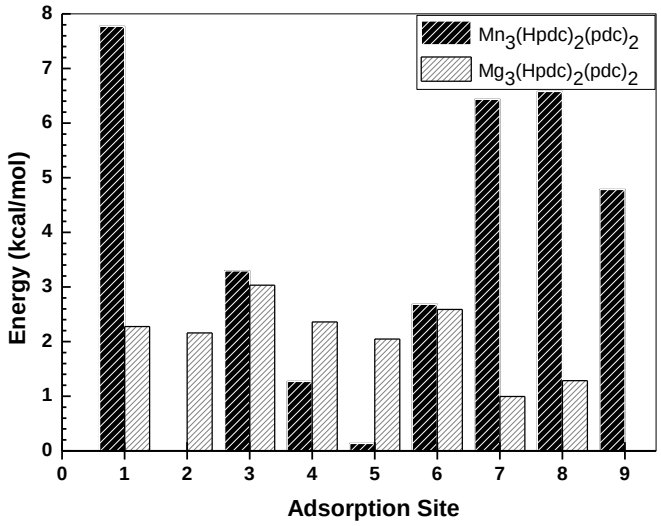

Figure 9. Comparison of interaction energy between single CO_2 molecule adsorption at different sites in $[Mn_3(Hpdc)_2(pdc)_2]$ **1** (black) and $[Mg_3(Hpdc)_2(pdc)_2]$ **2** (grey).

between –10 and –8 eV. As the geometry and charge analysis indicates, in this site a redistribution of the charge in the CO_2 molecule occurs and it interacts with a framework in a such way, that the partially charged carbon $C^{\delta+}$ and oxygen $O^{\delta-}$ atoms of the adsorbed CO_2 are aligned to ensure the most energetically favorable electrostatic interaction with the framework's partly charged nitrogen $N^{\delta-}$ and carbon $C^{\delta+}$ atoms (Figure S11, Table S4).

In case of compound **1** the manganese metal center plays a bigger role and therefore the adsorption has more complicated character and depends from the local charge distribution both in the framework and the guest molecule, involving some change of the charge at Mn atoms despite overall insignificant changes in the electronic structure (Figure S10). In this situation position 2 is more affordable. At this site, besides the alignment of negative $O^{\delta-}$ atoms of CO_2 in the proximity of partly positively charged carbon atoms of the framework, the guest molecule is also oriented to ensure the optimal distance to Mn(II) center (Figure S12, Table S5).

Overall, the differences in adsorption energies between nearest adsorption sites 1 and 2 for compound **1** are caused by the local atomic charge distribution in pyridinedicarboxylate ligands. The less stable CO_2 adsorption configuration for compound **1** at site 9 is made possible due to shorter distance between the molecule and the framework as opposed to compound **2**. This leads to electrostatic repulsion between oxygen atom (O_1) of CO_2 molecule and ligand's oxygen of the framework (O_7).

Furthermore, in the case of magnesium analogue **2**, the difference in energy lies near 3 kcal/mol indicating a rapid diffusion rate and more facile formation of the most thermodynamically affordable localization of CO_2 inside the pore. The binding of subsequent CO_2 molecules is accompanied by linear decrease in adsorption energy indicating a sorption pathway which is characteristic for type I isotherms, For **1**, however, the difference in the host-guest interaction energy compared at different CO_2 loadings reaches about 8 kcal/mol (Table 3). This suggests the presence of a particular diffusion barrier inside the pore at low CO_2 loadings and low temperatures. Therefore, a very pronounced step is observed in the experimental adsorption isotherm and can be explained by the delay in the formation of the chain due to a low diffusion rate of CO_2 within the MOF pore at temperatures below 235 K. At higher temperatures the permeability within the framework increases, and the guest molecules can readily move within the pores and thus form the most thermodynamically stable guest superstructure (Figure 8). This explains why **1** demonstrates typical type I adsorption isotherm at temperatures above 235 K.

Magnetic measurements of the framework **1** are another method to monitor the sorption process. Variable-temperature magnetic susceptibility measurements were performed over the temperature range 2–300 K and gave an effective magnetic moment value $\mu_{eff} = 9.77\ \mu_B$ for **1** at

300K, which is slightly lower than the spin-only value of 10.24 μ_B expected for three isolated paramagnetic high-spin Mn(II) ions (S = 5/2, g = 2) (Figure S13). Upon cooling, the value of the effective magnetic moment decreases continuously and reaches 5.78 μ_B at 2 K which is in a good agreement with a theoretical value of 5.92 μ_B for one paramagnetic Mn(II) ion (S = 5/2). The decrease of μ_{eff} values in **1** suggests antiferromagnetic interactions between the metal centers. The temperature-dependent magnetic susceptibility above 30K follows the Curie–Weiss law $\chi = C/(T - \theta)$. The plot of χ^{-1} vs T gives a Curie constant C = 13.22 $cm^3 \cdot K \cdot mol^{-1}$ and Weiss constant θ = – 30.32 K, slightly higher than values of known examples with similar composition.[58–60] The trimer model (spin-Hamiltonian $H = -2J(S_{Mn1}S_{Mn2}+S_{Mn2}S_{Mn3})$) was used for the analysis of the μ_{eff}(T) dependence for **1**. The best fit values of the g-factor and exchange coupling parameter *J* are 1.99 and -2.09 cm^{-1} (Figure S8).

Though Mg-containing analog **2** is not magnetically active, it is possible to partially substitute Mg centers in diamagnetic **2** with Mn(II) ions to generate the magnetically active $[Mn_xMg_{3-x}(Hpdc)_2(pdc)_2]$ containing low concentrations of magnetically active centers. This feature is very important for the investigation of CO_2 sorption in the Mn-diluted framework $[Mn_xMg_{3-x}(Hpdc)_2(pdc)_2]$ using EPR spectroscopy, which can monitor interactions between CO_2 and the Mn centres within the host framework. The EPR spectrum of activated Mn-doped **2** contains 6 lines (Figure S14). Introduction of 1 CO_2 molecule slightly changes the shape of the peaks, and the observed broadening suggests a change in the strains (local distributions) of the hyperfine interaction constants either on N and Mn or solely on N centers. It should be noted that DFT simulations also revealed that the formation of the CO_2 chain superstructure starts at the adsorption sites close to pyridine N-centres (Figure S7). Thus, EPR spectroscopic data bring good experimental evidence for the theoretical simulations.

N centers can effectively interact with CO_2 due to the high quadrupole moment of this gas, and therefore we argued that **1** and **2** may show selectivity to CO_2 over N_2 and CH_4. Sorption/desorption isotherms for N_2 and CH_4 were recorded at 273 and 298 K and compared with corresponding isotherms for CO_2 (Figure S15). Both **1** and **2** have low N_2 capacity at ambient conditions, and the N_2 uptake does not exceed 7 mL/g even at 273 K and 1 bar. The selectivity for CO_2/N_2, defined as the ratio between the Henry constants (Table S6) are especially high for **2** at 49.8 at 273 K and 30.5 at 298 K. The selectivity for CO_2/N_2 increases with increasing temperature for **1** from 4.6 at 273 K to 18.9 at 298 K; we have observed a similar effect for other N-containing MOFs in the case of C_2H_2 *vs* CO_2 selectivity.[34] This may indicate that even at relatively high temperatures the guest-guest interactions for CO_2 still strongly affect the sorption mechanism and modulate host-guest interactions. In **2** the sorption process is mostly governed by host-guest interactions and especially between the N-centres of the pzc^{2-} ligand and guest CO_2. This results in a higher selectivity and a characteristic decrease of selectivity with increasing temperature. N_2 molecules interact weakly with both frameworks in **1** and **2** and with each other; thus, the observed selectivity is mostly dependent upon the CO_2 adsorption energetics.

To model the performance of **1** and **2** in the separation of binary mixtures we also calculated the selectivity using ideal adsorbed solution theory (IAST) (Figure S16).[61] For 1:1 CO_2/N_2 mixtures at 1 bar the selectivity factor for **1** is 2.8 at 273 K and 4.5 at 298 K; for **2** they are 23.5 at 273 K and 19 at 298 K. This analysis revealed good performance for **2** for CO_2 extraction from mixtures with low (less than 20%) CO_2 content. As expected, **1** has somewhat lower selectivity for CO_2 capture in comparison to **2** at low concentrations of CO_2.

The separation of CO_2 and CH_4 is another important industrial process. Both **1** and **2** demonstrate good performance in CO_2/CH_4 separation with selectivity factors reaching 8.0 at 273 K for **2** at 273 K and 1 bar (Table S7) based upon Henry's constant calculation. The selectivity factors decrease with temperature for both compounds (from 7.6 to 7.4 for **1**, and from 8.0 to 7.2 for **2**) 273K and 1 bar. Interaction of CH_4 with MOF surfaces is stronger than for N_2, and therefore the Henry's constant for adsorption of CH_4 is strongly temperature dependent. It also results in lower selectivity for CO_2 than N_2. The calculated enthalpy of adsorption at zero coverage is 26.0 and 24.5 $kJ \cdot mol^{-1}$for CO_2, and 25.3 and 21.8 $kJ \cdot mol^{-1}$ for CH_4 for **1** and **2**, respectively.

IAST calculations also confirm that due to the higher energy of the CH_4–MOF interaction, the selectivity of both compounds to CO_2 is lower than for N_2 mixture (Figure S17). For 1:1 CO_2/CH_4 at 1 bar the selectivity factors for **1** are 2.8 at 273 K and 2.5 at 298 K, and 8.7 at 273K and 9 at 298 K for **2**.

CONCLUSIONS

Two metal-organic frameworks with unique adsorption properties have been prepared. The compounds show a high selectivity for CO_2 with a very broad S-shaped hysteresis observed for CO_2 adsorption in **1**. Theoretical modelling revealed the formation of unique chain CO_2 superstructures within the channels of these porous compounds and confirmed the presence of 4 adsorption sites at low CO_2 loadings for both compounds. Though their spatial arrangement is similar in both structures, the order in which local sites are filled by CO_2 varies for each compound, resulting in significant differences in host-guest energetics. As a result a high

diffusion barrier emerges in case of **1** which results in the observed S-shaped sorption isotherm. The theoretical calculations are supported experimentally by magnetic and EPR studies.

ASSOCIATED CONTENT

Supporting information for this article is given via the link at the end of this document.

AUTHOR INFORMATION

Corresponding Author

E-mail: sergei.sapchenko@manchester.ac.uk.

Author Contributions

[#]The first two authors contributed equally to this research work.

ACKNOWLEDGMENTS

The reported study was funded by RFBR according to the research project № 18-29-04001. R.V.B. is grateful to the crew of Center for Computational Materials Science and E-IMR center at the Institute for Materials Research, Tohoku University, for continuous support and also thankful to the Ministry of Education, Culture, Sports, Science, and Technology of Japan (Grant No. 17H03122) for financial support. EPR studies were supported by FASO (0333-2017-0002). A.M.S thanks RF President's grant MK-3272.2017.3 and FASO (0333-2017-0002). M.S. acknowledges support from the ERC (AdG 742041).

REFERENCES

1. https://public.wmo.int/en/media/press-release/greenhouse-gas-concentrations-surge-new-record.

2. UNEP (2016). The Emissions Gap Report 2016. United Nations Environment Programme (UNEP), Nairobi.

3. Wang, S.; Yan, S.; Ma, X.; Gong, J. Recent advances in capture of carbon dioxide using alkali-metal-based oxides. *Energy Environ. Sci.*, **2011**, *4*, 3805–3819.

4. Bang, Y.; Han, S.-J.; Kwon, S.; Hiremath, V.; Song, I.-K.; Seo, J.-G. High Temperature Carbon Dioxide Capture on Nano-Structured $MgO–Al_2O_3$ and $CaO–Al_2O_3$ Adsorbents: An Experimental and Theoretical Study. *J. Nanosci. Nanotechno.*, **2014**, *14*, 8531–8538.

5. Wang, K.; Zhao, P.; Guo, X.; Hai, D.; Chao, Y. High-temperature CO_2 capture cycles of hydrated limestone prepared with aluminum (hydr)oxides derived from kaolin. *Energ. Convers. Manage.*, **2014**, *86*, 1147–1153.

6. Dobrova, E. P.; Bratchikova, I. G.; Mikhalenko, I. I. Adsorption of carbon dioxide on tantalum oxide coated with palladium chloride. *Russ. J. Phys. Chem.*, **2006**, *80*, 1528–1531.

7. Nambo, A.; He, J.; Nguyen, T. Q.; Atla, V.; Druffel, T.; Sunkara, M. Ultrafast Carbon Dioxide Sorption Kinetics Using Lithium Silicate Nanowires. *Nano Lett.*, **2017**, *17*, 3327–3333.

8. Choi, S.; Drese, J.; Jones, C. Adsorbent Materials for Carbon Dioxide Capture from Large Anthropogenic Point Sources. *Chem. Sus. Chem.*, **2009**, *2*, 796–854.

9. Kosinov, N.; Gascon, J.; Kapteijn, F.; Hensen, E. J. M. Recent developments in zeolite membranes for gas separation. *J. Membrane Sci.*, **2016,** *499*, 65–79.

10. Majchrzak, A.; Nowak, W. Separation characteristics as a selection criteria of CO_2 adsorbents. *Journal of CO_2 Utilization*, **2017**, *17*, 69–79.

11. Sreenivasulu, B.; Sreedhar, I.; Venugopal, A.; Reddy, B. M.; Raghavan, K. V. Thermokinetic Investigations of High Temperature Carbon Capture Using a Coal Fly Ash Doped Sorbent. *Energ. Fuel.*, **2017**, *31*, 785–794.

12. Rashidi, N. A.; Yusup, S. An overview of activated carbons utilization for the post-combustion carbon dioxide capture. *Journal of CO_2 Utilization*, **2016**, *13*, 1–16.

13. Adelodun, A. A.; Kim, K.-H.; Ngila, J. C.; Szulejko, J. A review on the effect of amination pretreatment for the selective separation of CO_2. *Appl. Energ.*, **2015**, *158*, 631–642.

14. Zhang, Z.; Yao, Z.-Z.; Xiang, S.; Chen, B. Perspective of microporous metal–organic frameworks for CO_2capture and separation. *Energ. Environ. Sci.*, **2014**, *7*, 2868–2899.

15. Chaemchuen, S.; Kabir, N. A.; Zhou, K.; Verpoort, F. Metal–organic frameworks for upgrading biogas *via* CO_2adsorption to biogas green energy. *Chem. Soc. Rev.*, **2013**, *42*, 9304–9332.

16. Belmabkhout, Y.; Guillerm, V.; Eddaoudi, M. Low concentration CO_2 capture using physical adsorbents: Are metal–organic frameworks becoming the new benchmark materials? *Chem. Eng. J.*, **2016**, *296*, 386–397.

17. Abu Ghalia, M.; Dahman, Y. Development and Evaluation of Zeolites and Metal–Organic Frameworks for Carbon Dioxide Separation and Capture. *Energy Technology*, **2017**, *5*, 356–372.

18. Sreenivasulu, B.; Sreedhar, I.; Suresh, P.; Raghavan, K. V. Development Trends in Porous Adsorbents for Carbon Capture. *Environ. Sci. Technol.*, **2015**, *49*, 12641–12661.

19. Zhou, K.; Chaemchuen, S.; Verpoort, F. Alternative materials in technologies for Biogas upgrading via CO_2 capture. *Renew. Sust. Energ. Rev.*, **2017**, *79*, 1414–1441.

20. Zeng, Y.; Zou, R.; Zhao, Y. Covalent Organic Frameworks for CO_2 Capture. *Adv. Mater.*, **2016**, *28*, 2855–2873.

21. Olajire, A. A. Recent advances in the synthesis of covalent organic frameworks for CO_2 capture. *Journal of CO_2 Utilization*, **2017**, *17*, 137–161.

22. Vicent-Luna, J. M.; Luna-Triguero, A.; Calero, S. Storage and Separation of Carbon Dioxide and Methane in Hydrated Covalent Organic Frameworks. *J. Phys. Chem. C*, **2016**, *120*, 23756–23762.

23. McDonald, T. M.; Mason, J. A.; Kong, X.; Bloch, E. D.; Gygi, D.; Dani, A.; Crocellà, V.; Giordanino, F.; Odoh, S. O.; Drisdell, W. S.; Vlaisavljevich, B.; Dzubak, A. L.; Poloni, R.; Schnell, S. K.; Planas, N.; Lee, K.; Pascal, T.; Wan, L.F.; Prendergast, D.; Neaton, J.B.; Smit, B.; Kortright, J. B.; Gagliardi, L.; Bordiga, S.; Reimer, J. A.; Long, J. R. Cooperative insertion of CO_2 in diamine-appended metal-organic frameworks. *Nature*, **2015**, *519*, 303–308.

24. Bruker Advanced X-ray Solutions; Bruker AXS Inc.: Madison, WI, **2004**.

25. Sheldrick, G. M. Crystal structure refinement with SHELXL. *Acta Crystallogr., Sect. C: Struct. Chem.*, **2015**, *71*, 3–8.

26. Spek, A. L. PLATON SQUEEZE: a tool for the calculation of the disordered solvent contribution to the calculated structure factors. *Acta Crystallogr., Sect. C: Struct. Chem.*, **2015**, *71*, 9–18.

27. Kresse, G.; Furthmüller, J. Efficiency of ab-initio total energy calculations for metals and semiconductors using a plane-wave basis set. *Comput. Mater. Sci.*, **1996**, *6*, 15–50.

28. Kresse, G.; Furthmüller, J. Efficient iterative schemes for *ab initio* total-energy calculations using a plane-wave basis set. *Phys. Rev. B*, **1996**, *54*, 11169–11186.

29. Perdew, J. P.; Burke, K.; Ernzerhof, M. Generalized Gradient Approximation Made Simple. *Phys. Rev. Lett.*, **1996**, *77*, 3865–3868.

30. Blöchl, P. E. Projector augmented-wave method. *Phys. Rev. B*, **1994**, *50*, 17953–17979.

31. Monkhorst, H. J.; Pack, J. D. Special points for Brillouin-zone integrations. *Phys. Rev. B*, **1976**, *13*, 5188–5192.

32. Grimme, S. Semiempirical GGA-type density functional constructed with a long-range dispersion correction. *J. Comput. Chem.*, **2006**, *27*, 1787–1799.

33. Momma, K.; Izumi, F. *VESTA 3* for three-dimensional visualization of crystal, volumetric and morphology data *J. Appl. Crystallogr.*, **2011**, *44*, 1272–1276.

34. Sapchenko, S. A.; Dybtsev, D. N.; Samsonenko, D. G.; Belosludov, R. V.; Belosludov, V. R.; Kawazoe, Y.; Schröder, M.; Fedin, V. P. Selective gas adsorption in microporous metal–organic frameworks incorporating urotropine basic sites: an experimental and theoretical study. *Chem. Commun.*, **2015**, *51*, 13918–13921.

35. Dybtsev, D. N.; Yutkin, M. P.; Samsonenko, D. G.; Fedin, V. P.; Nuzhdin, A. L.; Bezrukov, A. A.; Bryliakov, K. P.; Talsi, E. P.; Belosludov, R. V.; Mizuseki, H.; Kawazoe, Y.; Subbotin, O. S.; Belosludov, V. R. Modular, Homochiral, Porous Coordination Polymers: Rational Design, Enantioselective Guest Exchange Sorption and Ab Initio Calculations of Host–Guest Interactions. *Chem. Eur. J.*, **2010**, *16*, 10348–10356.

36. Tang, W.; Sanville, E.; Henkelman, G. A Grid-Based Bader Analysis Algorithm without Lattice Bias. J. Phys.: Condens. Matter, **2009**, *21*, No. 084204.

37. Sanville, E.; Kenny, S. D.; Smith, R.; Henkelman, G. An Improved Grid-Based Algorithm for Bader Charge Allocation. J. Comput. Chem., **2007**, *28*, 899−908.

38. Henkelman, G.; Arnaldsson, A.; Jónsson, H. A Fast and Robust Algorithm for Bader Decomposition of Charge Density. Comput. Mater. Sci., **2006**, *36*, 354−360.

39. Yu, M.; Trinkle, D. R. Accurate and Efficient Algorithm for Bader Charge Integration. J. Chem. Phys., **2011**, *134*, No. 064111.

40. Brown, I. D. The Chemical Bond in Inorganic Chemistry: The Bond Valence Model, Oxford University Press, 2002.

41. Wei, Y.; Yu, Y.; Wu, K. Highly Stable Five-Coordinated Mn(II) Polymer $[Mn(Hbidc)]_n$ (Hbidc=1H-Benzimidazole-5,6-dicarboxylate): Crystal Structure, Antiferromegnetic Property, and Strong Long-Lived Luminescence. *Cryst. Growth. Des.*, **2008**, *8*, 2087–2089.

42. Bai, Y.; Gao, H.; Dang, D.-B.; Guo, X.-Y.; An, B.; Shang, W.-L. A series of metal–organic frameworks based on polydentate Schiff-base ligands derived from benzil dihydrazone: synthesis, crystal structures and luminescent properties. *Cryst. Eng. Comm.*, **2010**, *12*, 1422–1432.

43. Ju, P.; Jiang, L.; Lu, T.-B. A Three-Dimensional Dynamic Metal–Organic Framework with Fourfold Interpenetrating Diamondoid Networks and Selective Adsorption Properties. *Inorg. Chem.*, **2015**, *54*, 6291–6295.

44. Bezuidenhout, C. X.; Smith, V. J.; Bhatt, P. M.; Esterhuysen, C.; Barbour, L. J. Extreme Carbon Dioxide Sorption Hysteresis in Open-Channel Rigid Metal–Organic Frameworks. *Angew. Chem. Int. Ed.*, **2015**, *54*, 2079 –2083.

45. Henke, S.; Schneemann, A.; Wutscher, A.; Fischer, R. A. Directing the Breathing Behavior of Pillared-Layered Metal–Organic Frameworks via a Systematic Library of Functionalized Linkers Bearing Flexible Substituents. *J. Am. Chem. Soc.*, **2012**, *134*, 9464−9474.

46. Dau, P. V.; Kim, M.; Garibay, S. J.; Münch, F. H. L.; Moore, C. E.; Cohen, S. M. Single-Atom Ligand Changes Affect Breathing in an Extended Metal–Organic Framework. *Inorg. Chem.*, **2012**, *51*, 5671−5676.

47. Hwang, I. H.; Bae, J. M.; Hwang, Y.-K.; Kim, H.-Y.; Kim, C.; Huh, S.; Kim, S.-J.; Kim, Y. CO_2 selective dynamic two-dimensional Zn^{II}coordination polymer. *Dalton Trans.*, **2013**, *42*, 15645–15649.

48. Yang, S.; Lin, X.; Lewis, W.; Suyetin, M.; Bichoutskaia, E.; Parker, J. E.; Tang, C. C.; Allan, D. R.; Rizkallah, P. J.; Hubberstey, P.; Champness, N. R.; Thomas, K. M.; Blake, A.J.; Schröder, M. A partially interpenetrated metal-organic framework for selective hysteretic sorption of carbon dioxide. *Nat. Mater.*, **2012**, *11*, 710–716.

49. Wang, J.; Luo, J.; Zhao, J.; Li, D.-S.; Li, G.; Huo, Q.; Liu, Y. Assembly of Two Flexible Metal–Organic Frameworks with Stepwise Gas Adsorption and Highly Selective CO_2 Adsorption. *Cryst. Growth Des.*, **2014**, *14*, 2375−2380.

50. Saha, R.; Kumar, S. {[Co_2(ndc)$_2$(bpee)$_2$](bpee)}: a 3D multifunctional MOF. *Cryst. Eng. Comm.*, **2012**, *14*, 4980–4988.

51. Orcajo, G.; Calleja, G.; Botas, J. A.; Wojtas, L.; Alkordi, M. H.; Sanchez-Sanchez, M. Rationally Designed Nitrogen-Rich Metal–Organic Cube Material: An Efficient CO_2 Adsorbent and H_2 Confiner. *Cryst. Growth Des.*, **2014**, *14*, 739−746.

52. Mulfort, K. L.; Farha, O. K.; Malliakas, C. D.; Kanatzidis, M. G.; Hupp, J. T. An Interpenetrated Framework Material with Hysteretic CO_2Uptake. *Chem. Eur. J.*, **2010**, *16*, 276–281.

53. Mu, B.; Li, F.; Huang, Y.; Walton, K.S. Breathing effects of CO_2 adsorption on a flexible 3D lanthanide metal–organic framework. *J. Mater. Chem.*, **2012**, *22*, 10172–10178.

54. Samsonenko, D. G.; Kim, H.; Sun, Y.; Kim, G.-H.; Lee, H.-S.; Kim, K. Microporous Magnesium and Manganese Formates for Acetylene Storage and Separation. *Chem. Asian J.*, **2007**, *2*, 484–488.

55. Dybtsev, D. N.; Chun, H.; Yoon, S. H.; Kim, D.; Kim, K. Microporous Manganese Formate: A Simple Metal−Organic Porous Material with High Framework Stability and Highly Selective Gas Sorption Properties. *J. Am. Chem. Soc.*, **2004**, *126*, 32–33.

56. Walton, K. S.; Millward, A.R.; Dubbeldam, D.; Frost, H.; Low, J.L.; Yaghi, O. M.; Snurr, R. Q. Understanding Inflections and Steps in Carbon Dioxide Adsorption Isotherms in Metal-Organic Frameworks. *J. Am. Chem. Soc.*, **2008**, *130*, 406–407.

57. Valenzano, L.; Civalleri, B.; Sillar, K.; Sauer, J. Heats of Adsorption of CO and CO_2 in Metal–Organic Frameworks: Quantum Mechanical Study of CPO-27-M (M = Mg, Ni, Zn). *J. Phys. Chem. C*, **2011**, *115*, 21777–21784.

58. Wang, X.-W.; Dong, Y.-R.; Zheng, Y.-Q.; Chen, J.-Z. A Novel Five-Connected BN Topological Network Metal−Organic Framework Mn(II) Cluster Complex. *Cryst. Growth Des.*, **2007**, *7*, 613–615.

59. Zheng, Y.-Q.; Xu, W.; Zhu, H.-L.; Lin, J.-L.; Zhao, L.; Dong, Y.-R. New pyridine-2,4,6-tricarboxylato coordination polymers: Synthesis, crystal structures and properties. *Cryst. Eng. Comm.*, **2011**, *13*, 2699–2708.

60. Ren, P.; Chen, P.-K.; Xu, G.-F.; Chen, Z. Novel $(4^2 \cdot 8^4)(4^3 \cdot 6^3)_2(4^6 \cdot 6^3 \cdot 8^6)_2$ topology network built up from the highly connective pyridine-2,4,6-tricarboxylate ligand. *Inorg. Chem. Commun.*, **2007**, *10*, 836–838.

61. Myers, A. L.; Prausnitz, J. M. Thermodynamics of mixed-gas adsorption. *AlChE J.*, **1965**, *11*, 121–127.

TOC Synopsis

Pair of new isostructural microporous coordination frameworks $[Mn_3(Hpdc)_2(pdc)_2]$ (**1**) and $[Mg_3(Hpdc)_2(pdc)_2]$ (**2**) (pdc^{2-} = pyridine-2,4-dicarboxylate) demonstrates completely different sorption behavior. While compound **2** has a typical type I shape CO_2 isotherm, **1** features a two-step adsorption process with a very broad hysteresis between the adsorption and desorption curves. The combination of DFT calculations, sorption and XRD analysis explains this effect showing differences in host-guest and guest-guest interactions during CO_2 adsorption process.

TOC Graphic

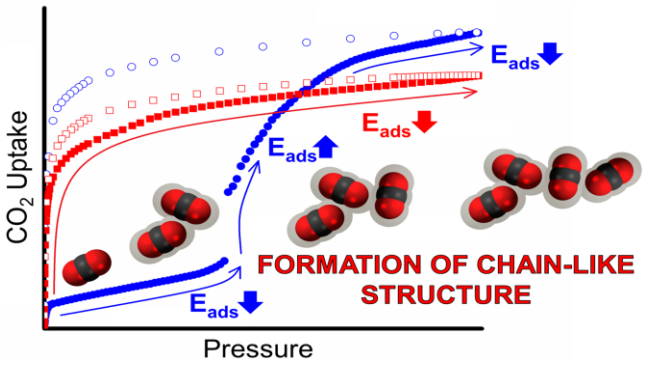
CO_2 Uptake
Pressure
E_{ads}
E_{ads}
E_{ads}
E_{ads}
FORMATION OF CHAIN-LIKE STRUCTURE